World Electric Vehicle Journal

Article

Personalized Path-Tracking Approach Based on Reference Vector Field for Four-Wheel Driving and Steering Wire-Controlled Chassis

Changhua Dai [1,*], Changfu Zong [2], Dong Zhang [3,*], Hongyu Zheng [2], Chuyo Kaku [4], Dingheng Wang [1] and Kai Zhao [1]

[1] Northwest Institute of Mechanical and Electrical Engineering, Xianyang 712000, China
[2] State Key Laboratory of Automotive Simulation and Control, Jilin University, Changchun 130022, China
[3] Department of Mechanical and Aerospace Engineering, Brunel University London, Middlesex UB8 3PH, UK
[4] Jiangsu Chaoli Electric Co., Ltd., Danyang 212321, China
* Correspondence: changhuadai@163.com (C.D.); dong.zhang@brunel.ac.uk (D.Z.)

Abstract: It is essential and forward-thinking to investigate the personalized use of four-wheel driving and steering wire-controlled unmanned chassis. This paper introduces a personalized path-tracking approach designed to adapt the vehicle's control system to human-like characteristics, enhancing the fit and maximizing the potential of the chassis' multi-directional driving and steering capabilities. By modifying the classic vehicle motion controller design, this approach aligns with individual driving habits, significantly improving upon traditional path-tracking control methods that rely solely on reference vector fields. First, the classic reference vector field's logic was expanded upon, and it is shown that a personalized upgrade is feasible. Then, driving behavior data from multiple drivers were collected using a driving simulator. The fuzzy c-means clustering method was used to categorize drivers based on typical states that match vehicle path-tracking performance. Additionally, the random forest algorithm was used as the method for recognizing driving style. Subsequently, a personalized path-tracking control strategy based on the reference vector field was developed and a distributed execution architecture for four-wheel driving and steering wire-controlled unmanned chassis was established. Finally, the proposed personalized path-tracking approach was validated using a driving simulator. The results of the experimental tests demonstrated that the personalized path-tracking control approach not only fits well with various driving styles but also delivers high accuracy in driving style identification, making it highly suitable for application in four-wheel driving and steering wire-controlled chassis.

Keywords: wire-controlled unmanned chassis; personalized path-tracking; reference vector field; driving style identification

Citation: Dai, C.; Zong, C.; Zhang, D.; Zheng, H.; Kaku, C.; Wang, D.; Zhao, K. Personalized Path-Tracking Approach Based on Reference Vector Field for Four-Wheel Driving and Steering Wire-Controlled Chassis. *World Electr. Veh. J.* **2024**, *15*, 198. https://doi.org/10.3390/wevj15050198

Academic Editor: Joeri Van Mierlo

Received: 3 April 2024
Revised: 18 April 2024
Accepted: 19 April 2024
Published: 3 May 2024

1. Introduction

As an ideal chassis form for intelligent vehicles, the four-wheel driving and steering (4WDaS) wire-controlled chassis has great potential for unmanned maneuverability. The four-wheel drive of a 4WDaS wire-controlled chassis is achieved by four independent wheels driven-by-wire, with each wheel capable of varying driving torque outputs. Additionally, four-wheel steering is realized via steer-by-wire technology, employing four independent steering motors capable of rotating the wheels up to 180 degrees in either direction. Path-tracking control is the direct interface layer between the 4WDaS wire-controlled chassis and the intelligent driving system. As the basic foundation of intelligent driving technology, the path-tracking control layer has a direct impact on the final performance of intelligent vehicles. Scholars and researchers have proposed a variety of path-tracking technologies to better achieve the driver's desired driving target [1,2], including geometric and kinematic algorithms, dynamic control algorithms, optimization algorithms, adaptive

control algorithms, model-based algorithms, and classical algorithms, etc. [3,4]. Personalized driving strategies can reduce the driver discomfort associated with generic-style control. Notably, variations in drivers' gender, driving experiences, and ages lead to distinct driving behaviors, even under identical conditions [5]. Consequently, personalized driving strategies have become one of the hotpots in intelligent transportation control research [6,7]. However, since the 4WDaS wire-controlled chassis is predominantly utilized in unmanned transportation scenarios, there has been insufficient research into human-like path-tracking control for this type of chassis. It is necessary to conduct anthropomorphic research on the multi-dimensional characteristics of 4WDaS wire-controlled chassis, which is particularly vital for meeting the requirements of Level 3 (L3) intelligent driving [8], aiming to achieve both strong maneuverability and high user acceptance.

Currently, the personalized path-tracking methods available are predominantly tailored for conventional vehicle chassis designs. For example, Qu proposed a method for modeling driver steering behavior based on the characteristics of parameter changes in a driver–vehicle–road closed-loop system. The model uses a random model predictive control method to facilitate personalized path-tracking control [9]. Li et al. introduced two different learning-based personalized driver models to predict the preview distance based on the pure pursuit algorithm, which achieved good path-tracking performance [10]. Despite these advancements, research into personalized path-tracking is still in its early stages, with methodologies largely adhering to more traditional approaches. In the above studies, the driving styles of drivers were usually divided into three categories: cautious, general, and aggressive [11]. Specific control performance parameters were then designed to meet different driving styles. Therefore, the identification of driving styles has become a key area of research. In works on driving style recognition, the main research focuses on the selection and improvement of identification algorithms and the values of input features. For instance, Zhu et al. took the physiological characteristics of the driver as the parameters of driving style [12]. Other scholars have employed the interactive signals between drivers and vehicles as the parameters of driving style [9,13], while some researchers have focused on the vehicle running state as the parameters for driving style [14,15]. Although the review in [6] summarized many input characteristics, few are derived from the holistic running state of the vehicle. In autonomous vehicles, which lack human drivers, the difference between different styles lies in the running state of the vehicle. Therefore, relying on the characteristic values of traditional operable devices for driving style identification may not be directly applicable to 4WDaS wire-controlled chassis. Regarding driver identification and classification technology, the differences mainly lie in the employment of different identification methods; for example, neural network technology [14], and support vector machines (SVM) technology [16]. Due to the applicability and limitations of different algorithms, it is necessary and valuable to explore the application effects of different machine learning algorithms.

Path-tracking methods for 4WDaS wire-controlled chassis are often enhancements of traditional path-tracking algorithms, such as a multi-input multi-output nonlinear model predictive control [17] and a dynamic output feedback path-tracking controller based on robust $H\infty$ [18]. However, the above methods generally lack specificity for this type of chassis. Recently, a method based on the reference vector field (RVF) has entered the research field. This method is based on a reference velocity vector and has both lateral and longitudinal references, which can naturally match the multi-directional adjustment ability of the 4WDaS wire-controlled chassis. The path-tracking method based on RVF was proposed by Gordon [4]. The RVF method is a general framework for the action of an automated driver (or driver model) to provide both longitudinal and lateral control of a road vehicle. Because of its simple and efficient performance and the ability for quadratic planning, it has been widely studied by scholars, and even widely used in the field of aviation path-tracking [19]. However, most of the current path-tracking strategies prioritize tracking performance, without considering the driver's psychological acceptance of control [13]. In the context of autonomous vehicles, achieving driver psychological

acceptance of control is equally crucial alongside tracking performance. As drivers serve as the final operators and decision makers for vehicles, their psychological state directly affects their trust in and willingness to use the auto-drive systems. Therefore, optimizing the control strategy to make it more in line with the driver's driving habits and expectations can improve the driver's trust and willingness to use the auto-drive system, thereby improving the safety and reliability of the entire system. Studying the application of the path-tracking method based on RVF on a 4WDaS wire-controlled chassis is an effective attempt to combine the advantages of both approaches.

In summary, in order to enhance the driver's acceptance of the intelligent application of 4WDaS wire-controlled chassis, and to better align its path-tracking technology with the driver's personal driving style, this paper proposes a personalized path-tracking method based on RVF. First, the classic RVF was elaborated in detail and its potential for personalization was demonstrated. Second, a driving simulator was used to obtain driving behavior data from multiple drivers. Typical states corresponding to vehicle path-tracking performance were selected, and drivers were classified using the fuzzy c-means (FCM) clustering method. The random forest (RF) algorithm was used as the driving style identification method. Subsequently, a distributed execution architecture was established for 4WDaS wire-controlled unmanned chassis. Finally, the proposed personalized path-tracking method was validated through a driving simulator. The approach is shown in Figure 1, which consists of three layers considering the different drivers' driving styles in the path-tracking approach design and verification process.

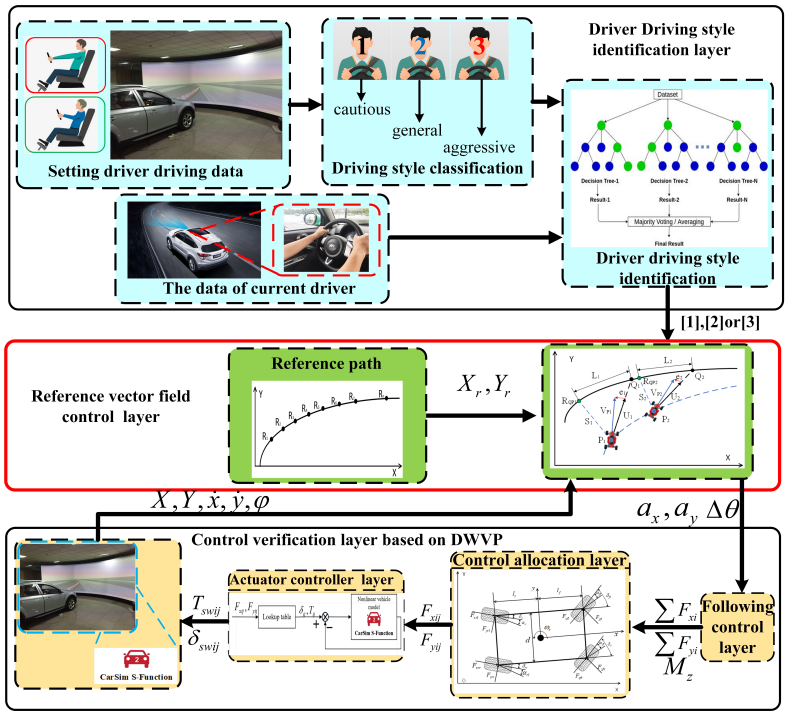

Figure 1. Approach diagram of the personalized path tracking approach.

The main contributions of this paper can be summarized as follows: (1) Introduction of vehicle level tracking states as features for driving style identification and the integration of FCM and RF algorithms to obtain accurate identification results. The driving style identification scheme is adapted to the characteristics of 4WDaS wire-controlled unmanned chassis; (2) Proposal of a personalized path-tracking algorithm based on RVF for 4WDaS wire-controlled chassis. The algorithm achieves adaptive extension of the RVF algorithm and enhances tracking performance across different driving styles.

The study is organized into the following sections: Section 2 conducts a feasibility reasoning proof of personalized path-tracking control based on RVF. Section 3 uses a

driving simulator to collect driving data and complete the classification and identification of driving styles. Section 4 builds the control architecture of a 4WDaS wire-controlled chassis. Section 5 relies on a driving simulator to verify the RVF-based 4WDaS wire-controlled chassis path-tracking algorithm. Section 6 presents the conclusions.

2. Feasibility Analysis for Personalized Path-Tracking Approach Based on RVF

The RVF-based path-tracking approach stands out for its simplicity and efficiency. The speed difference between the current and reference speed vectors is transformed into a demand for lateral and longitudinal acceleration, resulting in lateral and longitudinal forces, as well as steering angle control for the vehicle. The characteristic of generating both the wheel target driving force and wheel target steering angle naturally corresponds to the characteristics of the 4WDaS wire-controlled chassis.

2.1. Path-Tracking Approach Based on RVF

The movement of the vehicle on a plane is regarded as a two-dimensional movement, including both longitudinal and lateral movements. The position of the vehicle at point P is denoted as $P(X,Y)$, and its instantaneous speed is $\boldsymbol{V}_p(X,Y)$. As shown in Figure 2, throughout the driving process, the vehicle targets a reference point Q as the subsequent navigation objective.

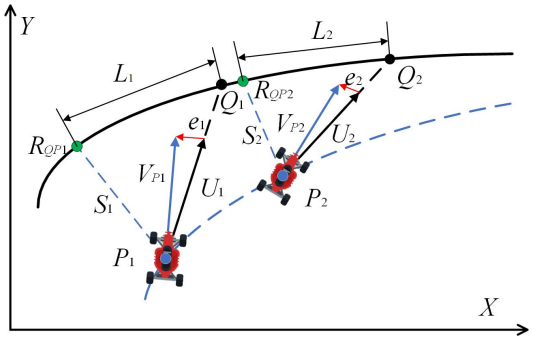

Figure 2. Schematic diagram of RVF.

The RVF operates by using the velocity vector U from point P to point Q as the reference velocity vector, while providing the reference direction and reference velocity magnitude. The vehicle then follows the reference speed and advances to point Q. As illustrated in Figure 3, each position of the vehicle correlates with a reference point on the target trajectory, forming countless velocity vectors that converge on the target trajectory. The field generated by countless velocity vectors will form the reference velocity vector field.

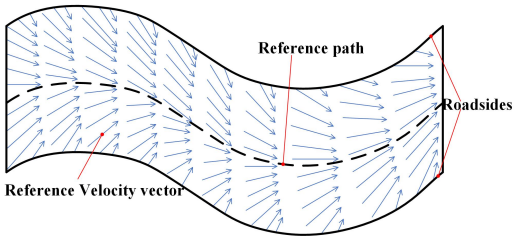

Figure 3. Schematic diagram of RVF convergence.

As the upper-level algorithm for path-tracking, RVF not only provides tracking control targets but also performs simple secondary path planning. Referring to the derivation in reference [4], it can be inferred that, when the reference path is a straight line parallel to the X-axis, the reference velocity vector $\boldsymbol{U}_p$ of point P can be expressed as

$$\boldsymbol{U}_p = \frac{u}{D}\begin{pmatrix} l \\ s \end{pmatrix}, \tag{1}$$

where l denotes the preview distance; s denotes the lateral distance between the vehicle and the reference path; u denotes the value of the reference speed; D denotes the distance from point P to Q; and $D = \sqrt{l^2 + s^2}$. Then, the following relationship can be derived:

$$\frac{\mathrm{d}X}{\mathrm{d}t} = \frac{ul}{D} \text{ and } \frac{\mathrm{d}Y}{\mathrm{d}t} = \frac{us}{D}, \tag{2}$$

Integrating the above equations, Equation (3) can be obtained:

$$Y = Y_0 \exp\left(\frac{X_0 - X}{l}\right), \tag{3}$$

where X_0 and Y_0 are the initial positions, respectively.

The obtained curve represents the vehicle's operating trajectory determined based on RVF. The trajectory converges to a straight line parallel to the $\boldsymbol{X}$-axis, which is different from the reference line trajectory. The above process is the simple secondary path planning function of RVF.

At point P, there is an error ($\boldsymbol{e}(t)$) between the current speed ($\boldsymbol{V}_p(t)$) and the reference speed ($\boldsymbol{U}_p$):

$$\mathbf{e}(t) = \boldsymbol{V}_p(t) - \boldsymbol{U}_p, \tag{4}$$

In order to ensure that the vehicle can converge to the target trajectory, the vehicle needs to travel in the direction of the reference speed. The vehicle's acceleration requirement at this moment is as follows:

$$\begin{aligned} \dot{\boldsymbol{e}}(t) &= \dot{\boldsymbol{V}}_p(t) - \dot{\boldsymbol{U}}(p_t) \\ &= \boldsymbol{a} - (\boldsymbol{V}_p \bullet \nabla)\boldsymbol{U} \\ &= \boldsymbol{a} - [(\boldsymbol{U} + \boldsymbol{e}) \bullet \nabla]\boldsymbol{U}, \end{aligned} \tag{5}$$

where $\nabla = (\frac{\partial}{\partial X}, \frac{\partial}{\partial Y})^T$, and

$$\nabla \bullet \boldsymbol{U} = \left(\frac{\partial \boldsymbol{U}_X}{\partial X} + \frac{\partial \boldsymbol{U}_Y}{\partial Y}\right). \tag{6}$$

A symmetric 2 × 2 matrix $\boldsymbol{H}$ instead of Equation (6):

$$\boldsymbol{H} = \begin{bmatrix} \frac{\partial \omega_X}{\partial X} & \frac{\partial \omega_Y}{\partial X} \\ \frac{\partial \omega_X}{\partial Y} & \frac{\partial \omega_Y}{\partial Y} \end{bmatrix} \tag{7}$$

For the symmetric 2 × 2 matrix $\boldsymbol{H}$, its eigenvalues ξ_1 and ξ_2 are real. Therefore, Equation (8) is satisfied:

$$\xi_1 + \xi_2 = \nabla \bullet \boldsymbol{U} = \left(\frac{\partial \boldsymbol{U}_X}{\partial X} + \frac{\partial \boldsymbol{U}_Y}{\partial Y}\right) \tag{8}$$

When the vehicle speed and the reference speed coincide, there are no initial errors:

$$\dot{\boldsymbol{e}}(t) = \boldsymbol{a} - (\boldsymbol{U} \bullet \nabla)\boldsymbol{U} = 0 \longrightarrow \boldsymbol{a} = \boldsymbol{a}_1(P(t)) \equiv (\boldsymbol{U} \bullet \nabla)\boldsymbol{U}. \tag{9}$$

Then, $\boldsymbol{a}_1$ denotes the acceleration to follow the change in the reference speed. This acceleration mainly reflects the change in the direction of the reference vehicle speed in the RVF; when the vehicle speed differs from the reference speed, an initial error occurs:

$$\dot{\boldsymbol{e}}(t) = \boldsymbol{a} - (\boldsymbol{U} \bullet \nabla)\boldsymbol{U} - (\boldsymbol{e} \bullet \nabla)\boldsymbol{U} \overset{\boldsymbol{a}=\boldsymbol{a}_1+\tilde{\boldsymbol{a}}}{\rightleftarrows} \dot{\boldsymbol{e}}(t) = \tilde{\boldsymbol{a}} - (\boldsymbol{e} \bullet \nabla)\boldsymbol{U} \tag{10}$$

$\tilde{\boldsymbol{a}}$ is used to eliminate the initial error caused by the mismatch of the current and reference vehicle speeds. To ensure the reliability of the controller, the acceleration $\tilde{\boldsymbol{a}}$ is limited to the friction circle, as shown in Figure 4:

$$|\tilde{\boldsymbol{a}}| \leq \varepsilon \leq \mu g \tag{11}$$

where ε is a positive real number smaller than μg. In order to eliminate the initial error $\boldsymbol{e}$, $\tilde{\boldsymbol{a}}$ needs to be processed as follows:

$$\tilde{\boldsymbol{a}} = \begin{cases} -\boldsymbol{e}, |\boldsymbol{e}| \leq \varepsilon \\ -\varepsilon \frac{\boldsymbol{e}}{|\boldsymbol{e}|}, |\boldsymbol{e}| > \varepsilon \end{cases} \tag{12}$$

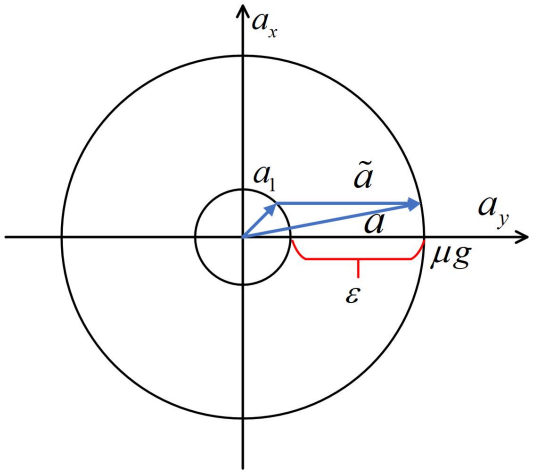

Figure 4. The schematic diagram of the friction circle constraint of the RVF.

Hence, Equation (13) is obtained:

$$e\dot{e} = \boldsymbol{e} \bullet \dot{\boldsymbol{e}} = \boldsymbol{e} \bullet \tilde{\boldsymbol{e}} - \boldsymbol{e} \bullet \left[(\boldsymbol{e} \bullet \nabla) \boldsymbol{U} \right] \tag{13}$$

where $e = (\boldsymbol{e} \bullet \boldsymbol{e})^{1/2}$ denotes the norm of $\boldsymbol{e}$. The second term may be simplified via the divergence matrix $\boldsymbol{H}$ in Equation (7):

$$\begin{aligned} e\dot{e} = \boldsymbol{e} \bullet \dot{\boldsymbol{e}} &= \boldsymbol{e} \bullet \tilde{\boldsymbol{a}} - \boldsymbol{e}^T \boldsymbol{H} \boldsymbol{e} \\ &\leq -e\varepsilon - \boldsymbol{e}^T (\xi_1 + \xi_2) \boldsymbol{e} \\ &= -e\varepsilon - (\xi_1 + \xi_2) e^2 \end{aligned} \tag{14}$$

Further simplifying Equation (14) yields Equation (15):

$$\dot{e} \leq -\varepsilon - (\xi_1 + \xi_2) e \tag{15}$$

When $\xi_1 + \xi_2 = 0$ and an initial error exists, the greatest derivative of the errors may be written as follows:

$$\dot{e} \leq -\varepsilon \tag{16}$$

Since the derivative of the error is bounded, when an initial error exists, the error will decrease to 0 during a finite period t_f, where the magnitude of t_f may be represented as

$$t_f = e/\varepsilon \tag{17}$$

As illustrated in Figure 3, after the vehicle reaches the acceleration $\tilde{\boldsymbol{a}}$, it will converge to the reference path.

Based on the above analysis, the neighboring reference vehicle speed variations throughout the whole RVF process are sufficiently minor to be disregarded, and hence the

a_1 may be ignored. The acceleration a will be utilized to eliminate the initial speed error, and the final control strategy is as follows:

$$a = \begin{cases} a, |a| \le \mu g \\ \mu g, |a| > \mu g \end{cases} \tag{18}$$

according to Equation (17), the target acceleration at the preview time can be obtained:

$$a = e/T \tag{19}$$

where T denotes the preview time, which is the fastest time to reach the reference speed when the preview point is known. By decomposing the acceleration into the longitudinal and lateral axes of the vehicle coordinate system, the target longitudinal acceleration a_x* and target lateral acceleration a_y* of the vehicle can be obtained.

2.2. Feasibility Analysis for RVF-Based Personalized Path Track Control

To assess the personalized feasibility based on RVF, this section explores the influence of RVF parameters on vehicle path tracking performance. First, a three-degree-of-freedom (3-DoF) vehicle model was established, incorporating various RVF parameters, such as the preview distance (preview time) and reference speed values. Subsequently, two sets of path-tracking experiments were conducted. In the simulation experiment, the vehicle was initiated from the point (0,0) and the target path was defined as a straight line with y = 3 m. The simulation research results, shown in Figure 5, indicated that

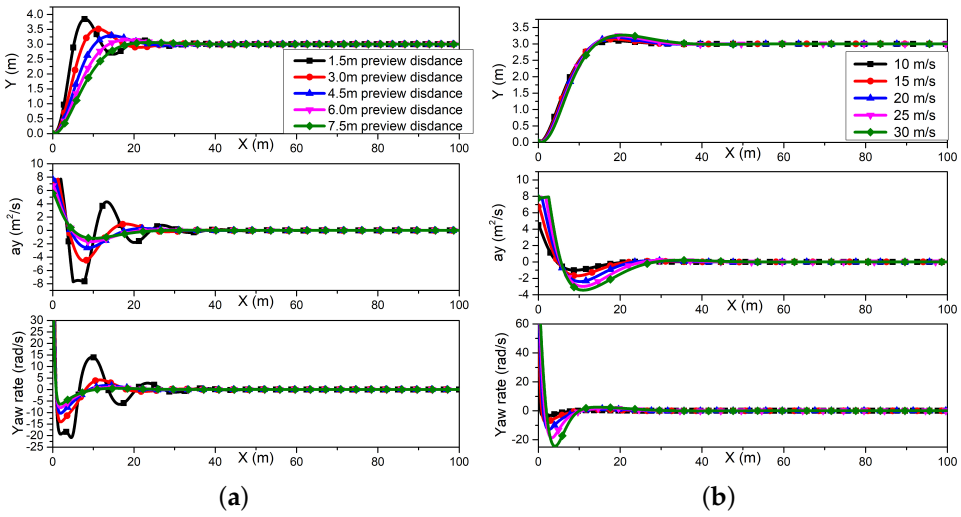

Figure 5. Simulation results; (**a**) 3-DoF vehicle simulation results with different preview distances; (**b**) 3-DoF vehicle simulation results with different reference velocities.

(1) With the reference vehicle speed set at 15 m/s and the preview distances being respectively 1.5 m, 3 m, 4.5 m, 6 m, and 7.5 m, it was observed that the maximum tracking error, maximum lateral acceleration, and maximum yaw rate all decreased as the preview distance increased.

(2) Conversely, when the preview distance was 6 m and the reference speeds were respectively 10 m/s, 15 m/s, 20 m/s, 25 m/s, and 30 m/s, the maximum tracking error, maximum lateral acceleration, and maximum yaw rate all increased with the increase in the reference speed.

According to the results of the preceding analysis, it is evident that when the other vehicle parameters were fixed, both the preview distance (preview time) and the reference speed values directly affected the path-tracking performance with RVF. Therefore, it can be concluded that by adjusting the preview distance (preview time) and reference speed

values of RVF, different effects on path-tracking performance could be achieved. Such insights form a theoretical basis for the personalized path-tracking approach.

3. Driving Style Classification and Identification

Given the feasibility of personalized path-tracking methods, this section details the collection of driving data and the classification and identification of driving styles. Unlike manned vehicles, where driving style features are often associated with the driver's operational characteristics, the selection of driving style features for unmanned chassis must avoid such driver-specific features. Therefore, this section focuses on solving driving style recognition based on non-operational features.

3.1. Driving Data Collection

For the driving data collection in this section, some typical steering test conditions were built in a driving simulator as shown in Figure 1. For this experiment, 64 drivers with different driving ages and different driving experiences were recruited for a set of path-tracking experiments. The experimental setup required each driver to navigate a predefined route within the simulator. All participants were given time to familiarize themselves with both the test bench and the driving scenarios before the tests, to ensure consistency in data collection. The drivers' driving behavior data and vehicle running state parameters were both collected during the experiment process. The collected data were filtered and processed via a data processing algorithm, and the feature value data of each driver were clustered into a set of data groups; hence 64 sets of feature value data were finally obtained.

3.2. Drivers' Driving Style Clustering

According to the collected dataset, the drivers were clustered based on their driving performance. Normally, a driver's driving style can be divided into three types: cautious, general, and aggressive drivers. Various data clustering algorithms are widely adopted, including RF, Markov networks, SVM, neural networks, K-means clustering, and other algorithms [20,21]. Among them, RF involves complicated steps, requiring careful selection of the kernel function. Similarly, adjusting parameters of an SVM can be challenging. Neural networks require strict parameter adjustments and may not guarantee convergence. The clustering quality of Markov networks and neural networks is not high. K-means is sensitive to outliers and initial values. However, due to its efficient and accurate clustering performance, unsupervised FCM usually does not require human intervention during algorithm implementation [22,23]. Therefore, this paper employed the FCM for driving data clustering. The FCM algorithm is a data clustering method based on the optimization of objective functions. The clustering result is the degree of membership of each data point to the clustering center, and the degree of membership can be represented by a numerical value.

Some researchers use driver input signals, such as steering wheel input signals, brake pedal signals, and accelerator pedal signals, as feature values for driving style classification. However, in terms of path tracking performance, a driver's driving style will ultimately manifest through how the vehicle's state influences its tracking performance. Cautious drivers pay more attention to safety and comfort during the driving process. When tracking a specific path, such a driver prefers to drive at a relatively low speed, and lateral accelerations and the tracking errors are usually small. In contrast, aggressive drivers focus more on maneuverability. They prefer higher speeds on the same paths, which typically results in higher lateral accelerations and larger tracking errors. General drivers balance safety with the vehicle's operational efficiency, so their performance generally falls between that of cautious and aggressive drivers.

Based on the above analysis, a driver's driving style is most apparent through various vehicle path-tracking states. First, these vehicle states more directly express the driver's operational intention. Second, focusing solely on driver inputs overlooks the impact of

the current working conditions. Different working conditions necessitate different driving inputs. Incorporating driver input feature values introduces the additional task of driving condition classification. Driver behavior is influenced by both the vehicle's state and work conditions; hence, simple driving operations alone cannot objectively describe the driver's driving style. Moreover, under different working conditions, the driver's input can interfere with style recognition. Hence, this paper classified the drivers' driving styles by considering the vehicle path tracking states as the feature values. To preserve the consistency between the vehicle path tracking states and the corresponding driver's driving style, the following feature values were collected: average vehicle speed, vehicle speed standard deviation, largest lateral acceleration, lateral acceleration standard deviation, largest yaw rate, yaw rate standard deviation, largest tracking error, and error standard deviation. Where the average speed, lateral acceleration, and yaw rate can reflect the driver's motion control demands. In addition, the path-tracking error is also an indispensable value to reflect the driver's path-tracking performance.

These features can be expressed as

$$f = \{e_1, e_2, ..., e_8\} \tag{20}$$

The clustering results based on the vehicle speed as the *X*-axis are shown in Figure 6.

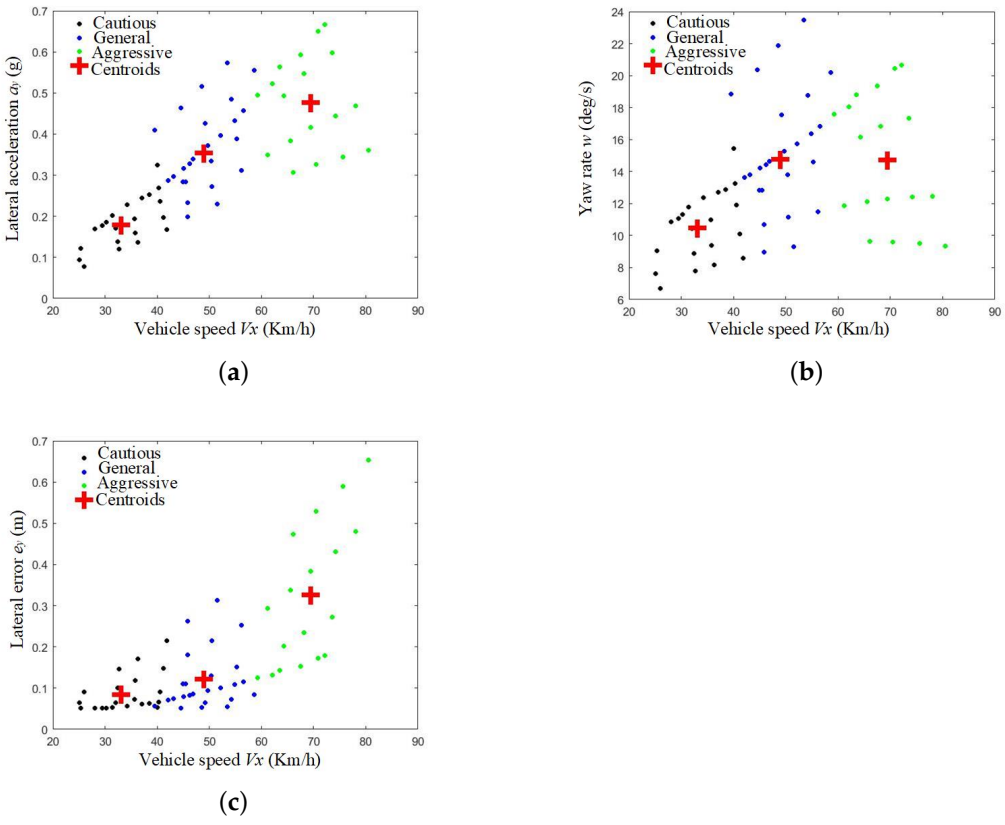

Figure 6. Clustering results; (**a**) lateral acceleration; (**b**) yaw rate; (**c**) lateral path-tracking error.

Figure 6 clearly shows the boundary between different clusters in the vehicle speed dimension, indicating that vehicle speed can well reflect the driver's driving style and is one of the key features. In addition, as shown in Figure 5, lateral acceleration and lateral path tracking error can well characterize driving behavior: as the vehicle speed increased, both lateral acceleration and lateral path tracking error also increased. According to the clustering results, the center speed of aggressive drivers could be set at 69.4 km/h, the center speed of general drivers could be set at 48.8 km/h, and the center speed of cautious

drivers could be set at 33.1 km/h. The relationship between vehicle speed and different driver types can thus be expressed as

$$u_a : u_g : u_c = 1.40 : 1 : 0.68 \tag{21}$$

The dataset with clustering marks then can be expressed as

$$X = \{e_{i1}, e_{i2}, ..., e_{i8}, c_i\}(i \in [1, 64]) \tag{22}$$

where e_{ij} denotes the i_{th} driver's j_{th} feature value, and c_i denotes the i_{th} driver's clustering mark.

3.3. Driver's Driving Style Identification

The current driver behavior identification algorithms generally include neural network identification, structural pattern identification, the statistical algorithm of pattern identification, and fuzzy identification [24–26]. Among these, it is difficult to select the meta-parameters and topology for neural networks. The neural network method relies heavily on data and exhibits poor real-time performance [27]. Structural identification tends to have a low recognition rate. The training set for the statistical algorithm of pattern identification is very important. It must be large and typical enough to ensure the reliability of the algorithm. Fuzzy identification relies heavily on membership functions. This paper employed the RF method, which has been proven to solve the problem that the data's randomness shows strong tolerance for outliers and interference, as the tool for driver driving style identification.

To verify the accuracy of the RF model, 60 sets were randomly selected from the 64 collected datasets to form the training set, while the remaining 4 datasets with known classification marks were used for testing and verification.

The following RF algorithm (Algorithm 1) could be obtained:

Algorithm 1. The Random Forest classification algorithm

Input: $I = (X, n)$, where $X = \{e_{i1}, e_{i2}, ..., e_{i8}, c_i\}(i \in [1, 64])$
1. 60 groups are randomly selected in X as the training set and the remaining 4 groups as the test set;
2. Sample from 60 groups with a Bootstrap method to randomly generate n training subsets and n decision trees;
3. Input parameters as Node Split Subsets. Select the optimal method according to the Least Square Error Criterion to split the nodes;
4. Each decision tree recursively grows from top to bottom and stops growing after satisfying the recursive termination condition. A1l combinations of decision trees constitute a random forest;
5. Enter the remaining 4 test data sets;
6. Select the highest number of votes as the corresponding classification mark of the driver $H(x) = \max \sum_{i=1}^{n} \phi(h_j(x) = y)$
Output: The final classification of 4 sets of test data sets with numbers 1 or 2, or 3.

3.4. Verification of Identification Accuracy

According to the model design, the test set was input into the trained RF for validation. The verification was repeated five times, and the results are shown in Table 1.

Table 1. Driver identification test results.

Number	Known Mark	Identification Mark	Accuracy
1	[2;1;3;3]	[2;1;3;3]	100%
2	[2;2;3;3]	[2;2;3;3]	100%
3	[2;3;3;2]	[2;3;3;2]	100%
4	[2;1;1;3]	[2;1;1;3]	100%
5	[1;2;3;1]	[1;2;3;2]	75%

The results indicate that the trained RF model had high identification accuracy and can be used for driver-style identification. In addition, the feasibility of selecting vehicle path tracking states as features was further verified.

4. Personalized Path-Tracking Approach and 4WDaS Wire-Controlled Chassis Modeling

4.1. Personalized Path-Tracking Approach Based on RVF

Based on the principles of RVF and the earlier identification of driver driving styles, this section designs a personalized path-tracking method based on RVF. The main parameters in RVF, including the preview distance (preview time) and reference speed, were adjusted according to the identified driving styles.

When tracking a specific path, the speed requirements vary among the three drivers types. The results of clustering showed that the speed performance of the cautious driver was lower, whereas the speed performance of the aggressive driver was higher, while the speed performance of the general driver fell in between. Hence, the design of a reference speed in RVF should be tailored to match these findings.

Given the varying speed requirements for different vehicles, the preview distance can be defined as the relative preview distance, which is the ratio of preview time to vehicle speed. This parameter more accurately reflects the driver's driving style, especially in terms of maintaining drivability during emergency situations. Cautious drivers, who prioritize safety, should have a longer relative preview distance. Conversely, aggressive drivers, who pay more attention to maneuverability, should have a shorter relative preview distance. The settings for general drivers should fall between these two extremes, balancing safety and maneuverability.

Assuming the current reference speed requirement is u_r. Based on the relationship of the center speeds obtained in the clustering results, the reference speed relationships for three types of driving styles can be obtained:

$$u_\mathrm{a} : u_\mathrm{g} : u_\mathrm{c} = 1.40u_\mathrm{r} : 1u_\mathrm{r} : 0.68u_\mathrm{r} \tag{23}$$

where u_a denotes the aggressive driver speed; u_g denotes the general driver speed; and u_c denotes the cautious driver speed.

At the same time, the preview time u_p can be set according to the reference vehicle speed and the proposed concept of the relative preview distance. In this paper, this could be set as

$$T_\mathrm{a} : T_\mathrm{g} : T_\mathrm{c} = T_\mathrm{p} : T_\mathrm{p} : T_\mathrm{p} \tag{24}$$

where T_a denotes the aggressive driver preview time; T_g denotes the general driver preview time; and T_c denotes the cautious driver preview time.

Hence, the absolute preview distance relationship among the three driver types can be obtained as

$$L_\mathrm{a} : L_\mathrm{g} : L_\mathrm{c} = 1.40 : 1 : 0.68 \tag{25}$$

where L_a denotes the aggressive driver absolute preview distance; L_g denotes the general driver absolute preview distance; and L_c denotes the cautious driver absolute preview distance. Note that this setting can satisfy the initial requirements of different drivers for absolute preview distance.

Then, the relative preview distance can be obtained as

$$L'_\mathrm{a} : L'_\mathrm{g} : L'_\mathrm{c} = 0.714 : 1 : 1.471 \tag{26}$$

where L'_a denotes the aggressive driver relative preview distance; L'_g denotes the general driver relative preview distance; and L'_c denotes the cautious driver relative preview distance. This setting can satisfy the requirements of different drivers for maintaining drivability during emergency driving situations.

Based on the clustering results collected from the driving simulator, the RVF parameter settings specific to the three identified driving styles were determined, allowing for tailored application enhancements based on RVF.

4.2. Hierarchical Execution Architecture for 4WDaS Wire-Controlled Unmanned Chassis

In order to verify the proposed personalized path tracking approach, a 4WDaS wire-controlled unmanned chassis based on a 3-DoF vehicle dynamic model is introduced in this section. All wheels of the 4WDaS wire-controlled unmanned chassis can be independently driven and steered, with decoupling achieved through controlled-by-wire technology.

As the control approach shows in Figure 1, the driver's driving style identification module provides classification results to the RVF control layer (where signal number 1 represents the cautious driver, signal number 2 represents the general driver, and signal number 3 represents the aggressive driver). Based on the identified driving style, the RVF control layer adjusts the preview distance and reference vehicle speed accordingly for the personalized path-tracking approach. In the meantime, the longitudinal and lateral accelerations, along with the vehicle speed vector errors can be obtained based on the RVF theory. In the subsequent control layer, the center forces for the lateral and longitudinal directions of the vehicle can be obtained based on the corresponding accelerations, and the desired vehicle yaw moment can be obtained by employing the sliding mode controller (SMC) that addresses the speed vector errors. The model operates under the assumption that the road surface is flat and disregards the vehicle's vertical motion and aerodynamic influences. Hence, the 3-DoF simplified vehicle dynamic model can be used for the control allocation layer. The linear-quadratic programming (LQP) method is introduced to distribute the total vehicle center forces and torque into the individual tire forces with a nonlinear friction circle constraint. Finally, in the actuator control layer, a SMC is employed to accurately track the desired tire steering angles and driving torques, as per the actuator control targets.

The vehicle acceleration is calculated in the upper-layer approach and decomposed into the vehicle's longitudinal and lateral directions. Consequently, the total forces in the longitudinal and lateral directions are determined according to Equation (27):

$$\begin{aligned} \sum F_{xi} &= ma_x \cos\varphi + ma_y \sin\varphi \\ \sum F_{yi} &= ma_y \cos\varphi - ma_x \sin\varphi \end{aligned} \tag{27}$$

where φ is the heading angle of the vehicle; m is the centroid mass; F_{xi} and F_{yi} are the longitudinal and lateral force of the i_{th} axle, respectively; and a_x and a_y are the longitudinal and lateral acceleration, respectively.

The initial direction error of the vehicle speed and the reference speed is known in the upper layer approach, and the yaw moment M_z is obtained by the SMC based on the heading angle error.

4.2.1. Control Allocation Layer

For simplicity, it is assumed that the road is flat, and both the vertical movement of the vehicle and the influence of aerodynamics are neglected.

The following Equation (28) describes the balancing force of the vehicle along the x-axis, y-axis, and z-axis:

$$\begin{cases} m\ddot{x} = m\dot{y}\dot{\rho} + \sum F_{xij} \\ m\ddot{y} = -m\dot{x}\dot{\varphi} + \sum F_{yij} \\ M_z = \boldsymbol{\Theta F} \end{cases} \qquad i = 1,2; j = 1,2 \tag{28}$$

where $\boldsymbol{F} = \begin{bmatrix} F_{x11} & F_{x12} & F_{x21} & F_{x22} & F_{y11} & F_{y12} & F_{y21} & F_{y22} \end{bmatrix}^T$;

$\boldsymbol{\Theta} = \begin{bmatrix} d & -d & d & -d & l_f & l_f & -l_r & -l_r \end{bmatrix}$; $\dot{x}$ and $\dot{y}$ are the longitudinal and lateral velocity, respectively; F_{xij} and F_{yij} are the longitudinal and lateral force of the ij_{th} wheel,

respectively; d is the half of the track width; and l_f and l_r are the distance from the center of mass to the front and rear axle, respectively.

Equation (29) indicates that the dynamic model of the 4WDaS wire-controlled unmanned chassis has four independent controllable force variables. In this paper, a LQP multi-objective optimization approach is employed for tire force allocation, with the following objective function:

$$\min|\boldsymbol{NF}-\boldsymbol{V}|^2 \tag{29}$$

where

$\boldsymbol{N}=\begin{bmatrix} a_{12} & a_{12} & a_{21} & a_{22} & -b_{11} & -b_{12} & -b_{21} & -b_{22} \\ b_{11} & b_{12} & b_{21} & b_{22} & a_{11} & a_{12} & a_{21} & a_{22} \\ c_{11} & c_{12} & c_{21} & c_{22} & d_{11} & d_{21} & d_{21} & d_{22} \end{bmatrix}$;

$a_{ij}=\cos\delta_{ij}$; $b_{ij}=(-1)^j d\cos\delta_{ij}+(-1)^{i+1}l_i\cos\delta_{ij}$; $c_{ij}=\sin\delta_{ij}$;

$d_{ij}=(-1)^{j+1}d\sin\delta_{ij}+(-1)^{i+1}l_i\cos\delta_{ij}$; $\boldsymbol{V}=\begin{bmatrix}\sum F_{xi} & \sum F_{yi} & M_z\end{bmatrix}^T$; δ_{ij} is the steering angle of the ij_{th} wheel.

At the same time, the cost function of LQP is converted into a standard function:

$$\min\left(\frac{1}{2}\tilde{\boldsymbol{x}}^T\boldsymbol{G}\tilde{\boldsymbol{x}}+\tilde{\boldsymbol{x}}^T\boldsymbol{c}\right) \tag{30}$$

where $\boldsymbol{c}$ is a constant matrix. Take the matrices $\boldsymbol{G}$ and $\tilde{\boldsymbol{x}}$ in the quadratic programming as

$$\boldsymbol{G}=\begin{bmatrix} 2\boldsymbol{N}^T\boldsymbol{N} & -2\boldsymbol{N} \\ -2\boldsymbol{N} & 2\boldsymbol{I} \end{bmatrix} \tag{31}$$

$$\tilde{\boldsymbol{x}}=\begin{bmatrix}\boldsymbol{F} & \boldsymbol{V}\end{bmatrix}^T \tag{32}$$

Proved to be

$$\begin{aligned} J&=\frac{1}{2}\begin{bmatrix}\boldsymbol{F}^T & \boldsymbol{V}^T\end{bmatrix}\begin{bmatrix}2\boldsymbol{N}^T\boldsymbol{N} & -2\boldsymbol{N}^T \\ -2\boldsymbol{N}^T & 2\boldsymbol{I}\end{bmatrix}\begin{bmatrix}\boldsymbol{F} \\ \boldsymbol{V}\end{bmatrix}+\begin{bmatrix}\boldsymbol{F}^T & \boldsymbol{V}^T\end{bmatrix}\begin{bmatrix}0 \\ 0\end{bmatrix} \\ &=\begin{bmatrix}\boldsymbol{F}^T\boldsymbol{N}^T\boldsymbol{N}-\boldsymbol{N}^T\boldsymbol{N} & -\boldsymbol{F}^T\boldsymbol{N}^T+\boldsymbol{V}^T\end{bmatrix}\begin{bmatrix}\boldsymbol{F} \\ \boldsymbol{V}\end{bmatrix} \\ &=\boldsymbol{F}^T\boldsymbol{N}^T\boldsymbol{N}\boldsymbol{F}-\boldsymbol{V}^T\boldsymbol{N}\boldsymbol{F}-\boldsymbol{F}^T\boldsymbol{N}^T\boldsymbol{V}+\boldsymbol{V}^T\boldsymbol{V} \\ &=(\boldsymbol{N}\boldsymbol{F}-\boldsymbol{V})^T(\boldsymbol{N}\boldsymbol{F}-\boldsymbol{V}) \\ &=\left|\boldsymbol{N}\boldsymbol{F}-\boldsymbol{V}\right|^2 \end{aligned} \tag{33}$$

When $\boldsymbol{c}=[0\ 0]^T$, it can be inferred from Equation (33) that Equation (29) is equivalent to Equation (30).

In the tire force allocation process, the lateral and longitudinal forces exerted on each tire must conform to the limits of the friction circle. As illustrated in Figure 7, the linear polygon constraint method is used to simplify the nonlinear friction circle constraint to solve the challenging and time-intensive nature of solving nonlinear constraint optimization problems. The specific constraints are as follows:

$$\begin{cases} |F_{xi}|\le\mu F_{zi} \\ |F_{yi}|\le\mu F_{zi} \\ |F_{xi}+F_{yi}|\le\sqrt{2}\mu F_{zi} \\ |F_{xi}-F_{yi}|\le\sqrt{2}\mu F_{zi} \end{cases} \tag{34}$$

where μ is the road adhesion coefficient; F_{zi} is the longitudinal force of the i_{th} axle.

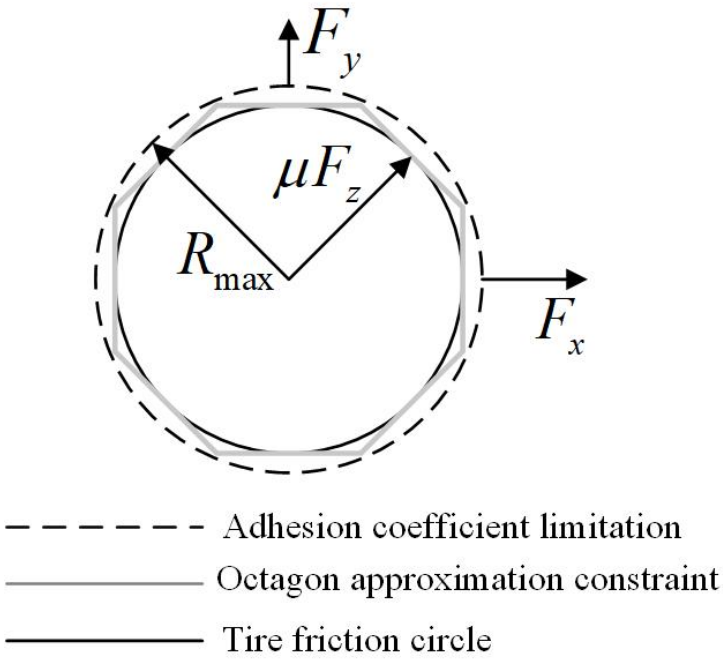

Figure 7. Schematic diagram of linear polygon friction circle constraint.

4.2.2. Actuator Control Layer

As a typical non-linear characteristic system, both the lateral and longitudinal forces exerted on the tire are non-linear and interconnected. The nonlinear Dugoff tire model and the magic tire model are widely used in tire models. The tire measurement data are listed in a lookup table, from which the longitudinal slip rate and tire side slip angle are obtained. Finally, the target wheel angle is calculated according to Equation (35), and the target torque is determined as shown in Equation (36).

$$\begin{bmatrix} \delta_{11} \\ \delta_{12} \\ \delta_{21} \\ \delta_{22} \end{bmatrix} = \begin{bmatrix} \alpha_{11} \\ \alpha_{12} \\ \alpha_{21} \\ \alpha_{22} \end{bmatrix} + \begin{bmatrix} \arctan\left(\frac{\dot{y}+l_f\dot{\varphi}}{\dot{x}-\dot{\varphi}d}\right) \\ \arctan\left(\frac{\dot{y}+l_f\dot{\varphi}}{\dot{x}+\dot{\varphi}d}\right) \\ \arctan\left(\frac{\dot{y}-l_f\dot{\varphi}}{\dot{x}-\dot{\varphi}d}\right) \\ \arctan\left(\frac{\dot{y}-l_f\dot{\varphi}}{\dot{x}+\dot{\varphi}d}\right) \end{bmatrix}, \tag{35}$$

$$T_{ij} = F_{xij} r_{\text{tire}} \tag{36}$$

where r_{tire} is the wheel radius; α_{ij} is the side slip angle of the ij_{th} wheel;T_{ij} is the target torque for the ij_{th} wheel. The independent driving and steering of 4WDaS are achieved through the layered architecture.

5. Simulation Verification of the Personalized Path-Tracking Approach Based on a Driving Simulator

5.1. Simulation Setup

In order to verify the proposed personalized path-tracking approach based on RVF, we used a high-fidelity driving simulator to establish a simulation test bench. A 4WDaS chassis model based on Simulink/Carsim was established for this purpose. Within the test platform, a 4WDaS wire-controlled unmanned chassis, modified using a C-class vehicle model within CarSim, was employed for the signal transformation. The drivers' driving signal were then computed within the Simulink/MATLAB environment. Due to the common occurrence of the double-lane change maneuver in real-word driving

scenarios, which includes both straight and curved phases, this could well reflect the driver's driving style. In addition, the data collected in Section 3 are also based on the double-lane change maneuver. Consequently, this section selected the classic double-lane change maneuver as the test condition. The experimental structure, as shown in Figure 1, was divided into two stages. The first stage involved driver driving style identification based on driving simulator operation, with the identification accuracy verification detailed in Section 3. The second stage focused on the verification of personalized path tracking control based on the results of the driver's driving style identification. Some key simulation parameters are outlined in Table 2. The running step of the simulation test was set to 1000 Hz.

Table 2. Simulation parameters.

Symbol	Variable Description	Value (Unit)
m	Total mass	1345 (kg)
I_Z	Moment of inertia	1523 (kg·m^2)
l_f	Distance from front axle to center of mass	1.01 (m)
l_r	Distance from rear axle to center of mass	1.46 (m)
d	Half of the track width	0.77 (m)
μ	Adhesion coefficient	0.8
C_f	Front axle lateral stiffness	62,900 (N.rad)
C_r	Rear axle lateral stiffness	62,900 (N.rad)

5.2. Simulation Results

According to the control approach shown in Figure 1, the results of the current driver identification were transmitted to the RVF control layer as numerical signals 1, 2, and 3. The controller then selected the relative preview distance and reference speeds corresponding to the identification results. This section verifies the personalized tracking performance of the three driving styles using a comprehensive set of recognition data. To better demonstrate the differences in path-tracking performance across the personalized tracking control strategies, the results are collectively analyzed and presented. For the purpose of the simulation, the reference speed u_{r} was set at 48.8 km/h according to the work conditions and the collected dataset. Then, based on Equation (25), the reference speeds for cautious, general, and aggressive drivers were set at 33.1 km/h, 48.8 km/h, and 69.4 km/h, respectively. In addition, the preview times for all types were standardized at 0.3 s. The results of the path-tracking test with three different driver driving styles are depicted in Figure 8.

The experimental results presented in Figure 8 offer a comprehensive comparison of the path-tracking control performance across different driving style identifications, including an evaluation of path-tracking control efficiency under varying states, as well as the operational performance of the 4WDaS wire-controlled unmanned chassis. In Figure 8a, the trajectories under three personalized tracking settings are displayed. The enlarged image indicates that there was little difference in trajectory tracking performance between the three settings, revealing tracking accuracy across speeds ranging from 33.1 km/h to 69.4 km/h. In specific, as depicted in Figure 8c, at vehicle speeds of 33.1 km/h, 48.8 km/h, and 69.4 km/h, the absolute values of the maximum lateral path tracking error were 0.20 m, 0.169 m, and 0.138 m, respectively. The lateral errors remained relatively small under the three personalized tracking settings. Figure 8b–e respectively show the key tracking states of the entire vehicle. Noticeable disparities were observed in the vehicle states across the three driving styles, effectively reflecting distinct driving behaviors. Specifically, as shown in Figure 8b, the absolute values of maximum lateral acceleration corresponding to cautious, general, and aggressive driving styles were 0.163 g, 0.327 g, and 0.594 g, respectively. It is common practice for researchers to set 0.4 g as the critical value for vehicle lateral acceleration. Therefore, in this test, the vehicle's driving state underwent a transition from a stable state to an extreme state.

As shown in Figure 8d, the absolute values of the maximum yaw rate corresponding to cautious, moderate, and aggressive driving styles were 1.59 deg/s, 4.22 deg/s, and 11.75 deg/s, respectively. This result proves that the controlled vehicle exhibited a more aggressive performance with the increase in target reference speed, which correspondingly reflected the requirements of the different drivers' driving styles. Figure 8e illustrates the side slip angle for the different driving styles. The absolute values of the maximum side slip angle corresponding to cautious, moderate, and aggressive driving styles were 12.46 deg, 13.69 deg, and 16.32 deg, respectively. As an important indicator of vehicle stability, the increasing body-side slip angles also reflected the distinct requirements of the different drivers' driving styles. Figure 8f presents the vehicle speed performance. Under the three tracking scenarios, the controlled vehicle was able to maintain the target reference speed with relatively small errors. Specifically, when operating in pure steering mode, there was a slight decrease in vehicle speed to accommodate the required lateral and longitudinal accelerations. However, the controlled vehicle increased the vehicle speed to the reference value in the short term to meet the longitudinal acceleration required by the upper controller. These minor speed fluctuations served as indicators of the longitudinal path-tracking capacity of the proposed algorithm. The results outlined above demonstrated the path-tracking states of different driving styles, with high-precision tracking effects and significant differences in overall vehicle states. Compared with Figure 6, the vehicle states under different styles conformed to the data collection rules.

Figure 8g–i respectively show the total longitudinal force, total lateral force, and yaw torque before and post LQP allocation. Under the different driving styles, except for the initial start-up, the target total force and allocated total force were basically consistent, achieving commendable tracking and execution. The above three subgraphs demonstrated the execution capability of the 4WDaS wire-controlled unmanned chassis. The results proved the effectiveness of the 4WDaS wire-controlled unmanned chassis execution based on LQP force distribution and a control layer. Meanwhile, the variation in demand for driving force and torque across the different driving styles corroborated the chassis's ability to adapt to personalized driving performances.

Combining the accuracy verification performance of driving style recognition in Section 3 with the diverse performances based on personalized RVF in Figure 8, the results indicate that the 4WDaS unmanned chassis using the personalized path-tracking approach proposed in this article could accurately identify the driver's driving style and achieve personalized path-tracking control performance. In summary, the proposed path tracking control approach not only reflected the driving style of the identified driver but also ensured high-precision path-tracking performance under various driving conditions, thereby meeting individual personalized driving intentions and requirements.

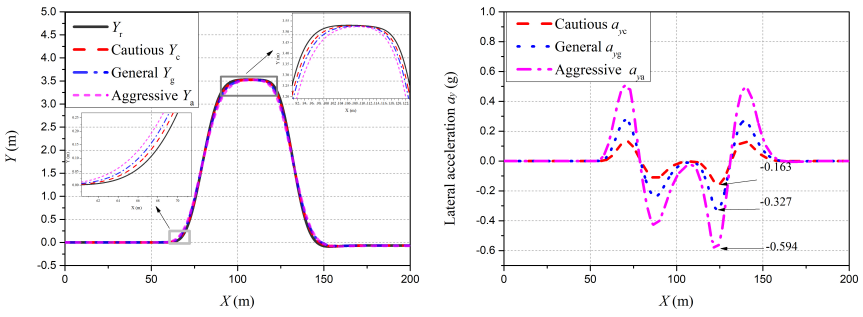

(**a**) (**b**)

Figure 8. *Cont.*

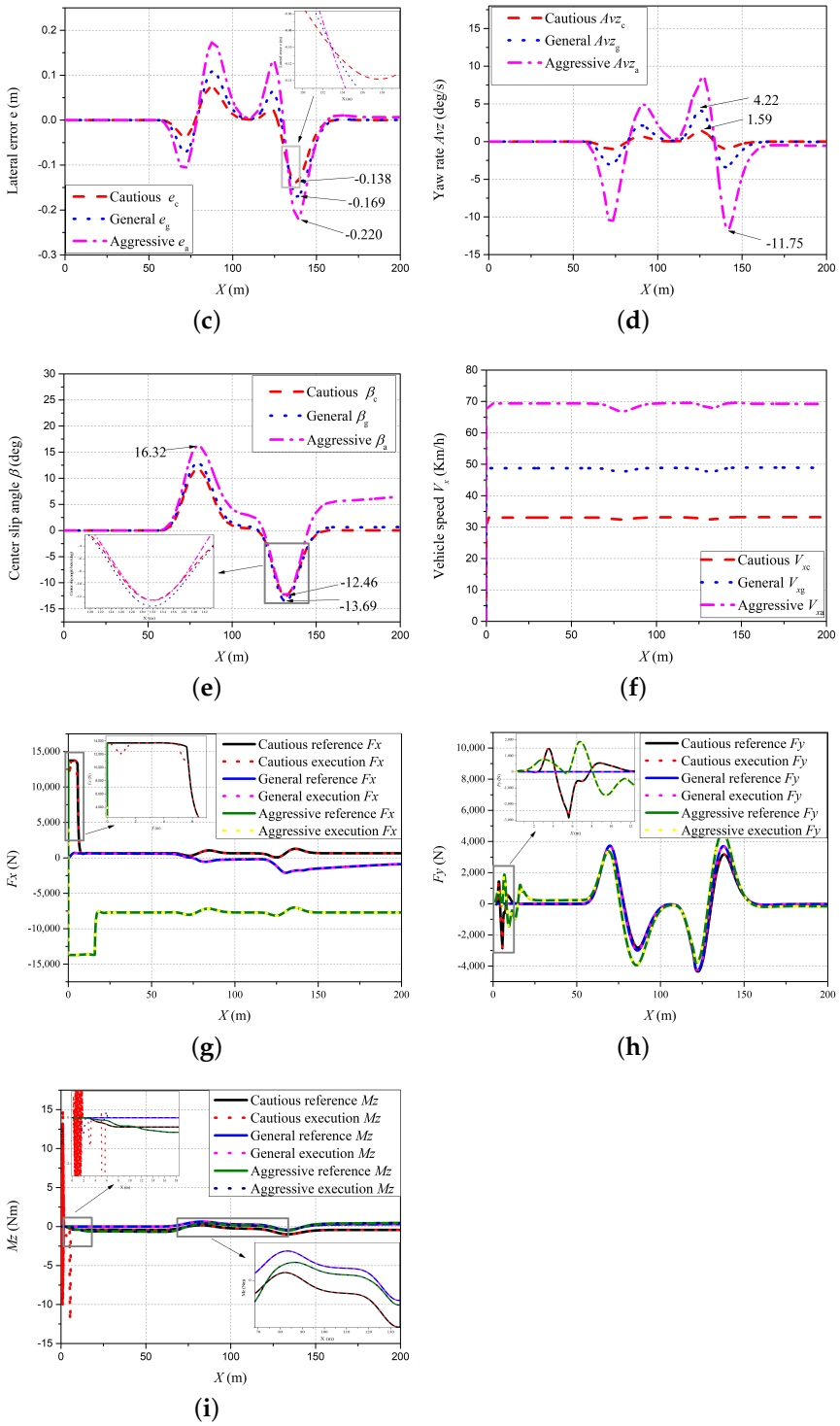

Figure 8. Simulation results; (**a**) Path-tracking trajectories; (**b**) lateral accelerations; (**c**) lateral errors; (**d**) yaw rates; (**e**) vehicle side slip angles; (**f**) vehicle speeds; (**g**) longitudinal forces; (**h**) lateral forces; (**i**) yaw torques.

6. Conclusions

This paper proposed a personalized trajectory tracking algorithm based on RVF for 4WDaS wire-controlled unmanned chassis. The classic RVF was reasonably extended, and the driving behavior data of multiple drivers were obtained using a driving simulator. For driving style identification, the fuzzy c-means clustering method coupled with the random forest algorithm was employed. The proposed personalized path-tracking

approach was validated through simulation testing. The experimental test results demonstrated that the personalized path-tracking control approach not only fit well with the 4WDaS wire-controlled unmanned chassis but also exhibited high accuracy in driving style identification, achieving effective personalized path-tracking performances. Furthermore, with the proposed personalized path-tracking approach, the vehicle could achieve a more human-like autonomous driving performance, to satisfy the design concept from "driver adapted to the car" to "car adapted to the driver".

It is important to note that the driving data used in this article were gathered using driving simulators, primarily to validate principles with minimal impact on the algorithm structure. In addition, the validation experiment in this article was based on data collection settings, and future research will explore the use of more extensive datasets to refine the clustering centers. There are still areas for further improvement in this article, such as the data sources and validation methods. Therefore, in future research will focus on applying and validating real vehicle data, to broaden the applicability and robustness of our findings.

Author Contributions: Conceptualization, C.D. and D.Z.; methodology, C.D.; software, C.D.; validation, C.D., D.Z. and C.Z.; formal analysis, D.Z.; investigation, H.Z.; resources, C.K., D.W. and K.Z.; data curation, C.D.; writing—original draft preparation, C.D.; writing—review and editing, C.D. and D.Z.; visualization, C.Z. and K.Z.; supervision, D.Z. and C.Z.; project administration, D.Z. and D.W.; funding acquisition, D.Z. and D.W. All authors have read and agreed to the published version of the manuscript.

Funding: This research was funded by Open Foundation of State Key Laboratory of Automotive Simulation and Control (Grant Number: 20201111); Major Scientific and Technological Innovation Project of Xianyang (Grant Number: L2023-ZDKJ-JSGG-GY-018).

Data Availability Statement: The data presented in this study are available on request from the corresponding author due to privacy.

Conflicts of Interest: Kaku Chuyo is an employee of Jiangsu Chaoli Electric Co. Ltd. The paper reflects the views of the scientists, and not the company.

References

1. Jiang, Y.; Deng, W.; Wu, J.; Zhang, S.; Jiang, H. Adaptive steering feedback torque design and control for driver–vehicle system considering driver handling properties. *IEEE Trans. Veh. Technol.* **2019**, *68*, 5391–5406. [CrossRef]
2. Chen, G.; Zhao, X.; Gao, Z.; Hua, M. Dynamic drifting control for general path tracking of autonomous vehicles. *IEEE Trans. Intell. Veh.* **2023**, *8*, 2527–2537. [CrossRef]
3. Amer, N.H.; Zamzuri, H.; Hudha, K.; Kadir, Z.A. Modelling and control strategies in path tracking control for autonomous ground vehicles: A review of state of the art and challenges. *J. Intell. Robot. Syst.* **2017**, *86*, 225–254. [CrossRef]
4. Gordon, T.J.; Best, M.C.; Dixon, P.J. An automated driver based on convergent vector fields. *Proc. Inst. Mech. Eng. Part D J. Automob. Eng.* **2002**, *216*, 329–347. [CrossRef]
5. Zhu, B; Chen, Y.; Zhao, J.; Su, Y. Design of an integrated vehicle platform control system with driver behavior identification. *Math. Probl. Eng.* **2015**, *2015*, 954514.
6. Martinez, CM.; Heucke, M.; Wang, F.; Gao, B.; Cao, D. Driving style recognition for intelligent vehicle control and advanced driver assistance: A survey. *IEEE Trans. Intell. Transp. Syst.* **2017**, *19*, 666–676. [CrossRef]
7. Wang, J.; Wang, J.; Wang, R.; Hu, C. A framework of vehicle trajectory replanning in lane exchanging with considerations of driver characteristics. *IEEE Trans. Veh. Technol.* **2017**, *66*, 3583–3596. [CrossRef]
8. Wiseman, Y. Autonomous vehicles. In *Encyclopedia of Information Science and Technology*, 5th ed.; IGI Global: Hershey, PA, USA, 2020; Volume 1, Chapter 1, pp. 1–11.
9. Qu, T. Driver Behavior Modeling Based on Stochastic Model Predictive Control. Ph.D. Thesis, Jilin University, Changchun, China, 2015.
10. Li, Z.; Wang, B.; Gong, J.; Gao, T.; Lu, C.; Wang, G. Development and evaluation of two learning-based personalized driver models for pure pursuit path-tracking behaviors. In Proceedings of the 2018 IEEE Intelligent Vehicles Symposium, Changshu, China, 26–30 June 2018; IEEE: Piscataway, NJ, USA, 2018; pp. 79–84.
11. Chu, D.; Deng, Z.; He, Y.; Wu, C.; Sun, C.; Lu, Z. Curve speed model for driver assistance based on driving style classification. *IET Intell. Transp. Syst.* **2017**, *11*, 501–510. [CrossRef]
12. Zhu, B.; Liu, Z.; Zhao, J.; Chen, Y.; Deng, W. Driver behavior characteristics identification strategies based on bionic intelligent algorithms. *IET Intell. Transp. Syst.* **2018**, *48*, 572–581. [CrossRef]
13. Liu, Y.; Zhang, D.; Gordon, T.; Li, G.; Zong, C. Approach of coordinated control method for over-actuated vehicle platoon based on reference vector field. *Appl. Sci.* **2017**, *9*, 297. [CrossRef]

14. Thitaree, T.; Chalermpol, S.; Suttipong, T. Combining unsupervised anomaly detection and neural networks for driver identification. *J. Adv. Transp.* **2017**, *2017*, 6057830.
15. Wang, W.; Xi, J.; Liu, C. Human-centered feed-forward control of a vehicle steering system based on a driver's path-following characteristics. *IEEE Trans. Intell. Transp. Syst.* **2016**, *18*, 1440–1453. [CrossRef]
16. Qian, H.; Ou, Y.; Wu, X.; Meng, X.; Xu, Y. Support vector machine for behavior-based driver identification system. *J. Robot.* **2010**, *2010*, 397865. [CrossRef]
17. Li, Y.; Cai, Y.; Sun, X.; Wang, H.; Jia, Y.; He, Y. Trajectory tracking of four-wheel driving and steering autonomous vehicle under extreme obstacle avoidance condition. *Veh. Syst. Dyn.* **2024** , *62*, 601–622. [CrossRef]
18. Li, Z.; Jiao, X.; Zhang, T. Robust H∞ Output Feedback Trajectory Tracking Control for Steer-by-Wire Four-Wheel Independent Actuated Electric Vehicles. *World Electr. Veh. J.* **2023** , *14*, 147. [CrossRef]
19. Jiang, W.; Wang, D.; Yin, W.; Ali, Z.A. UAV rendezvous based on time-varying vector fields. *Electron. Lett.* **2017**, *53*, 653–655. [CrossRef]
20. Wang, W.; Zhao, D.; Han, W.; Xi, J. A learning-based approach for lane departure warning systems with a personalized driver model. *IEEE Trans. Veh. Technol.* **2018**, *67*, 9145–9157. [CrossRef]
21. Xie, Y.; Murphey, Y. L.; Kochhar, D. Personalized driver workload estimation using deep neural network learning from physiological and vehicle signals. *IEEE Trans. Intell. Veh.* **2019**, *5*, 439–448. [CrossRef]
22. Lee,H.-E.; Park, K.-H.; Bien, Z.Z. Iterative fuzzy clustering algorithm with supervision to construct probabilistic fuzzy rule base from numerical data. *IEEE Trans. Fuzzy Syst.* **2008**, *16*, 263–277. [CrossRef]
23. Murugan, A.; Gobinath, D.; Kumar, S.G.; Muruganantham, B.; Velusamy, S. A time efficient and accurate retrieval of range aggregate queries using fuzzy clustering means (FCM) approach. *Int. J. Electr. Comput. Eng.* **2020**, *10*, 415. [CrossRef]
24. Ege, Y.; Nazlibilek, S.; Kakilli, A.; Citak, H.; Kalender, O.; Karacor, D.; Erturk, K. L.; Sengul, G. A study on the performance of magnetic material identification system by SIFT–BRISK and neural network methods. *J. Adv. Transp.* **2015**, *51*, 1–16. [CrossRef]
25. Hoshiya, M.; Saito, E. Structural identification by extended kalman filter. *J. Eng. Mech.* **1984**, *110*, 1757–1770. [CrossRef]
26. Ren, Q.; Baron, L.; Balazinski, M. Fuzzy identification of cutting acoustic emission with extended subtractive cluster analysis. *Nonlinear Dyn.* **2012**, *67*, 2599–2608. [CrossRef]
27. Abdolrasol, M.G.M.; Hussain, S.M.S.; Ustun, T.S.; Sarker, M.R.; Hannan, M.A.; Mohamed, R.; Ali, J.A.; Mekhilef, S.; Milad, A. Artificial neural networks based optimization techniques: A review. *Electronics* **2021**, *10*, 2689. [CrossRef]